Hybrid MPPT Method for Controlling an Open-Channel Hydrokinetic Microgenerator in Grid-Connected Mode

Edigar Nunes de Siqueira Júnior, Luigi Galotto Junior*, and Moacyr Aureliano Gomes de Brito

Faculty of Engineering, Architecture and Urbanism, and Geography
Federal University of Mato Grosso do Sul – UFMS
Campo Grande, MS, 79070-900, Brazil
*e-mail: luigi.galotto@ufms.br

***Abstract*—Hydrokinetic energy conversion has been gaining prominence among renewable energy sources due to its reasonable predictability and low environmental impact. In this context, this paper proposes the development of a maximum power point tracking (MPPT) algorithm for controlling a 10-kW hydrokinetic microgenerator in grid-connected mode. To maximize energy capture and ensure operational reliability, the strategy employs a hybrid process that uses the fixed-step "perturb and observe" (P&O) method to fine-tune the search within the high-efficiency region, established based on the unit's V–P (voltage–power) curve scan. The power stage consists of an in-stream turbine, a permanent magnet synchronous generator (PMSG), an uncontrolled rectifier, and a voltage source inverter. The control stage integrates the MPPT subsystem, along with a DC-link voltage regulator, output current compensators, phase-locked loops (PLLs), an islanding detector, and pulse width modulation (PWM) devices. The technique was validated using a simulation-based approach on the MATLAB/Simulink® platform, achieving an average tracking factor (TF) of 96.21% under varying flow conditions. Comparative results suggest that the algorithm makes the controller robust to small changes in plant parameters, such as those from mechanical wear, as the tolerance of the characteristic curve effectively mitigates their impact on the conversion rate.**

***Index Terms*—distributed generation, hydrokinetic conversion, islanding detection, MPPT technique.**

I. Introduction

HYDROELECTRICITY can be generated by either static or kinetic methods. In the first case, known as *hydrostatic conversion*, the gravitational potential energy is harnessed from water accumulated in large artificial reservoirs (dams). In the second case, known as *hydrokinetic conversion*, energy extraction is based simply on motion of any body of water, whether fresh or salt [1, 2].

With an estimated installed capacity of 1.3 TW, hydropower accounts for 16% of global electricity generation [2]. However, the share of large plants has practically remained stagnant over the last decade. The lack of new, potentially viable sites and the inherent risks have made investors prefer smaller ones [1]. Even so, financial and environmental issues have constituted a barrier to their expansion. Hydrokinetic conversion, on the other hand, has become popular. By not requiring dams and large infrastructure, stream generators tend to have lower implementation costs. Furthermore, they are considered to be environmentally friendly.

Regarding the operating principle, devices, and optimization techniques, hydrokinetic and wind turbines power plants are analogous [3]. However, physical and dynamic differences between exploited natural resources promote disparities in their structural and operational characteristics. For example, river turbines are generally less complex by not needing sensors and mechanisms for blade angle adjustment and rotor alignment [4]. Another important aspect is that even small units can have considerable capacity thanks to water's density, which is over 800 times denser than air. Moreover, their compact architecture allows for modularity and scalability [5].

Given the vast array of rivers, identifying the most suitable installation locations is crucial. In the absence of established norms and standards, site selection is based on several analytical criteria. The most suitable sections are those where the flow is relatively uniform throughout the year, with a minimal risk of flash floods, turbulence, or significant variations in speed or hydrometric level [6, 7].

To maximize energy capture, this work presents a maximum power point tracking (MPPT) algorithm for a grid-connected, open-channel hydrokinetic microgenerator. The proposed strategy is based on the perturb and observe (P&O) method and the unit's V–P (voltage–power) curve. This approach aims to provide stability and rapid convergence while preventing small variations in electrical and mechanical parameters from degrading the conversion rate.

This paper is organized into six sections. Following this introduction, Section II provides a theoretical foundation of

This paper was submitted for review on November 10, 2025.

the system. Section III reviews the relevant literature, and Section IV describes the methodology. The simulation results are presented in Section V, and Section VI offers concluding remarks.

II. Theoretical Framework

Fig. 1 shows the power and control stages of the open-channel hydrokinetic microgenerator. The power stage, represented on the top of the diagram, includes the following components: a turbine, a gearbox, a permanent magnet synchronous generator (PMSG), an uncontrolled rectifier, a capacitive filter, a three-phase inverter, and an inductive filter for grid connection. Its operation is based on the flow of water, which drives the turbine connected to the gear mechanism, increasing the angular speed to turn the rotor of the PMSG. The resulting AC power is then converted into DC power by the rectifier, which charges the DC-link capacitor. Finally, the inverter transfers the stored energy to the electrical grid via the connecting inductors. The control stage, illustrated on the bottom of the same diagram, is implemented by: an MPPT subsystem, voltage and current loops, phase-locked loops (PLLs), a slip mode frequency shift (SMS) islanding detector, and pulse width modulation (PWM) devices. Based on the output voltage and current of the rectifier (V_{DC} and I_{DC}, respectively), the MPPT algorithm generates the DC-link voltage reference (V_{DC}*) for the voltage loop, which in turn determines the output current amplitude (I_{peak}*) for the current loops. Then they define the respective modulation indices (m_A*, m_B*, m_C*) after receiving the grid's phase angles (θ_A*+δ_A, θ_B*+δ_B, θ_C*+δ_C), which are tracked by the PLLs and can be slightly disturbed by the islanding detectors. Finally, the modulating signals are processed via PWM to produce the trigger pulses for the inverter switches (g_1 to g_6).

A. Hydrokinetic Turbine

There are several concepts for harnessing the natural movement of water in open channels, but turbines are the most common, effective, and least invasive from an environmental perspective [3, 8]. Like wind devices, hydrokinetic turbines (HKTs) are driven by the velocity of the moving fluid, converting its kinetic energy into rotational mechanical power [9].

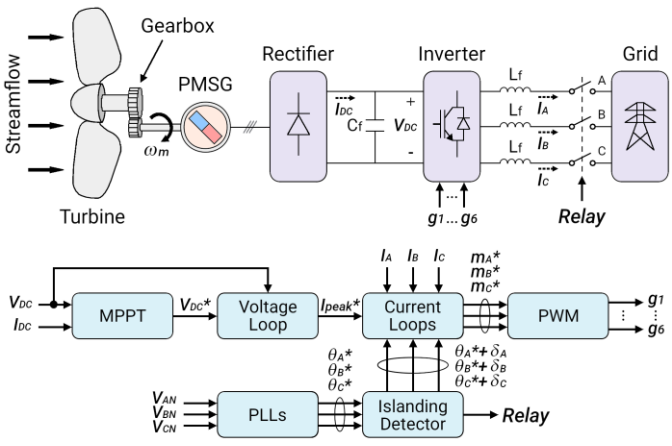

Fig. 1. Power and control stages of the open-channel hydrokinetic microgenerator (top and bottom, respectively).

Theoretically, unconfined (free) rotors cannot extract more than 59.3% of available energy, such coefficient is known as the "Betz limit." However, the efficiency of small-scale, in-stream turbines is much lower than this (approximately 25%) due to inherent losses. This factor, called coefficient of performance or power (C_p), is directly related to the tip speed ratio (TSR or λ) and the blade pitch angle (β) [10]. As freshwater currents are virtually unidirectional, adjusting the latter variable is unnecessary, which justifies the use of fixed-pitch mechanisms [11]. As a result, C_p is a function solely of λ, defined by

$$C_p(\lambda) = \frac{P_{mec}}{P_{hyd}}, \tag{1}$$

where P_{mec} is the mechanical power transferred to the shaft (W) and P_{hyd} is the available hydrokinetic power (W).

Since HKTs are governed by the same physical principles as wind systems, the mechanical power produced is likewise determined by

$$P_{mec} = \frac{1}{2}\rho A_T {V_F}^3 C_p(\lambda), \tag{2}$$

where ρ is the density of water (1000 kg/m^3), A_T is the rotor swept area (m^2), and V_F is the fluid speed (m/s).

Equation (2) implies that the amount of power grows with the cube of the flow speed, influencing the plant's revenue. Therefore, augmentation devices, e.g., ducts and diffusers, are commonly used to concentrate the fluid toward the turbine swept area [4].

Maximizing energy capture requires careful adjustment of the TSR. This dimensionless parameter expresses the mechanism hydrodynamic characteristics, relating the rotor peripheral speed to flow velocity, given as

$$\lambda = \frac{\omega_T R_T}{V_F}, \tag{3}$$

where ω_T is the turbine angular speed (rad/s) and R_T is the rotor radius (m).

Additionally, the mechanical torque can be obtained by using

$$T_{mec} = \frac{P_{mec}}{\omega_T}; \tag{4}$$

and the coefficient of torque can be expressed as

$$C_t(\lambda) = \frac{C_p(\lambda)}{\lambda}. \tag{5}$$

B. Permanent Magnet Synchronous Generator

PMSGs offer advantages in small-scale hydrokinetic systems because of simplicity, reliability, low noise, and power density [3]. However, such machines, originally designed to operate at constant speed, have to be connected to

power electronic converters to condition the energy produced at variable frequency [12].

To model a three-phase synchronous machine, Blondel's two-reaction theory is applied, which proposes the decomposition of armature magnetomotive force (MMF) into two fictitious rotating components: one aligned with the axis of the rotor magnetic poles, known as the direct-axis (or d-axis) component; and the other orthogonal to it, known as the quadrature-axis (or q-axis) component. According to this approach, the d-axis flux linkage (Ψ_d) of a conventional synchronous generator (SG) is the result of the superposition of fluxes from the d-axis stator current (i_d), the field winding current, and the rotor d-axis damper winding current. Similarly, the q-axis flux linkage (Ψ_q) is the sum of the superposition of fluxes from the q-axis stator current (i_q) and the rotor q-axis damper winding current [11]. Once a PMSG has no damper windings and the field coil is replaced by magnets, the dq-frame flux linkages are given as

$$\begin{cases} \Psi_d = L_d i_d - \Psi_{PM} \\ \Psi_q = L_q i_q \end{cases}, \tag{6}$$

where L_d and L_q are the stator dq-frame winding inductances (H), i_d and i_q are the previously mentioned currents (A), and Ψ_{PM} is the flux linkage produced by the permanent magnets (Wb) [13].

By applying the Kirchhoff method, the d-axis and q-axis terminal voltages of a permanent magnet synchronous machine in generator convention are derived as follows

$$\begin{cases} v_d = -R_s i_d - L_d \frac{di_d}{dt} + \omega_e L_q i_q \\ v_q = -R_s i_q - L_q \frac{di_q}{dt} - \omega_e (L_d i_d - \Psi_{PM}) \end{cases}, \tag{7}$$

where R_s is the resistance of each stator winding (Ω) and ω_e is the rotational electrical speed (rad/s), defined by

$$\omega_e = p.\omega_m = p.f_g.\omega_T, \tag{8}$$

where p is the number of pole pairs, ω_m is the rotational mechanical speed (rad/s), and f_g is the transmission ratio [14].

The previous parameters establish the electromagnetic torque on the generator shaft as

$$T_{em} = \frac{3p}{2}\left[\Psi_{PM} i_q - \left(L_d - L_q\right) i_d i_q\right]. \tag{9}$$

Reference [15] shows, moreover, that the active and reactive power delivered by a PMSG (i.e., a balanced three-phase system) can be expressed in the dq-frame, as demonstrated by

$$P = \frac{3}{2}\left(v_d i_d + v_q i_q\right), \tag{10}$$

$$Q = \frac{3}{2}\left(v_q i_d - v_d i_q\right). \tag{11}$$

III. Related Work

The following paragraphs provide a review of research on the efficiency and reliability of hydrokinetic power systems in recent decades.

An arrangement of three hydrokinetic generators supplying a resistive load connected to a DC bus was investigated to verify its performance under different scenarios [16]. Each generation unit consisted of a horizontal-axis turbine, a 10-kW PMSG, and a power electronics interface (PEI) made up of a passive rectifier bridge, an MPPT-based boost converter, and a buck converter for output voltage regulation. The study provided an analysis of the behavior of these multiple machines operating together, an approach seldom explored so far.

A control strategy for a fixed-pitch cross-flow turbine was presented, aiming to regulate its mechanical power [9]. The plant utilized a PMSG, an uncontrolled rectifier, and a boost converter connected to a DC microgrid. Producing 1.4 kW of electrical power at a rated water speed of 2.8 m/s, the system was fully linearized in the MATLAB/Simulink® environment and emulated through rotating machines and converters connected to a dSPACE® board. A key finding of the study was the comparison of two control methods: one based on power regulation mode (PRM) and the other using an MPPT algorithm.

A biogeography-based optimization (BBO) to obtain maximum power from a hydrokinetic device was proposed [17]. The technique, which establishes the parameters of proportional–integral (PI) compensators, was validated by employing a marine system model composed of a horizontal-axis turbine, a PMSG, and a back-to-back converter connected to the AC power grid. The system was simulated in MATLAB/Simulink® for discrete and stochastic flow variations. Although the authors did not report the converter voltage and current behavior, the results demonstrated the controller's accuracy, with the plant generating 15 kW at a stream speed of 2.8 m/s.

A vector control method applied to a grid-connected hydrokinetic microgenerator on the MATLAB/Simulink® platform was examined [5]. The system, which includes a Savonius turbine, a 7.5-kW induction generator (IG), an AC–DC–AC converter, and an LCL filter, was validated by varying the load characteristics (R and RL) and small input power variations. The plant produced 2 kW at a water flow of 1.5 m/s. However, it absorbed 4.5 kVAr from the electrical grid to maintain the machine's magnetic field.

Replacing an ordinary turbine, a vertical oscillator was used to harness energy from flowing water [18]. Seeking to integrate it into local microgrids, the researchers simulated, emulated, and field-tested the mechanism with a 7-kW PMSG and a two-stage PEI that included an uncontrolled rectifier bridge and an inverter. A constant output voltage was achieved under step and ramp variations in the generator speed by means of a proportional–integral–derivative (PID) control.

A study reported on the simulation of a low-capacity hydrokinetic generator following practical tests [19]. The system consisted of a current turbine, a PMSG, a three-phase

passive rectifier, an MPPT-based boost converter, and a buck converter controlled by the constant current–constant voltage (CC–CV) method. The model was run for a flow change from 0.83 m/s to 1.33 m/s, generating up to 105 W of power.

A hydrokinetic microgenerator designed for active power injection into the power grid was analyzed [20]. Using experimental data from a Pelton turbine, the unit included a PMSG, an uncontrolled full-bridge rectifier, and a single-phase inverter. An MPPT algorithm was embedded in the controller, and the system was validated in MATLAB/Simulink® for flow rates from 0.0018 m^3/s up to 0.0036 m^3/s, achieving a power output of 1.3 kW. Subsequently, the simulation was replicated for a horizontal-axis turbine. Crucially, the technique used to determine the operating points of the turbine–generator–rectifier (TGR) set was fundamental to the MPPT algorithm implemented in Section IV.

Simulation results in MATLAB/Simulink® confirmed the effectiveness of a vector control strategy for a hydrokinetic power plant [10]. The unit included a 2-kW PMSG, an in-stream turbine, and an AC–DC–AC converter, which featured a PWM rectifier, a boost converter, and an inverter. However, the simulation did not provide information on the voltages and currents between the converter stages, which limited further analysis.

The optimization of a hydrokinetic power system by directly regulating the output electrical currents was assessed [11]. The unit consisted of a horizontal-axis turbine coupled to a PMSG through a single-stage transmission. Applying a vector control technique to regulate the currents of an RL load, the model was run for flow speed from 1.5 m/s up to 3 m/s, achieving a power output of 380 kW. In the same work, the authors also discussed how the types of loads and the device's hydrodynamics affected the machine's behavior, impacting the plant's stability and efficiency.

IV. Methodology

The system was modeled in the MATLAB/Simulink® environment using the same HKT presented in [16], whose power coefficient curve is identified as

$$C_p(\lambda) = 0{,}007\lambda^4 - 0{,}026\lambda^3 - 0{,}158\lambda^2 + 0{,}655\lambda - 0{,}198. \quad (12)$$

The relationship between the turbine's energy conversion efficiency and its tip speed ratio is shown in Fig. 2. The blue curve illustrates that the maximum C_p of 0.39 is achieved at an *ideal* TSR of 1.79 for the device. Once the angular velocities of the turbine-generator set are intrinsically related to the DC-link voltage, it is possible to obtain the optimal operating condition by regulating the latter parameter via an MPPT algorithm. In addition to optimizing the process, this approach conveniently eliminates the need for external sensors, which are not only expensive but also relatively inaccurate [10]. The red curve in the same graph depicts the HKT's torque coefficient, which is derived from (5).

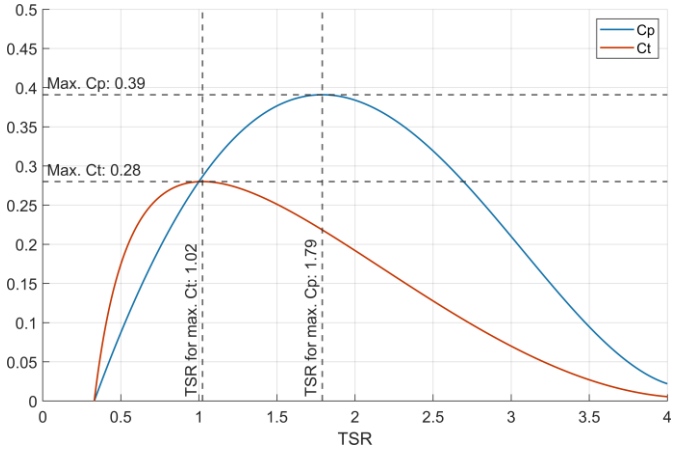

Fig. 2. Power and torque coefficient curves of the HKT.

Among several MPPT methods, the most widespread is known as "perturb and observe." Despite its simplicity and consistency, the technique with fixed-step size has some performance limitations, because convergence time and steady-state oscillation cannot both be satisfactory [19]. Therefore, combining P&O with another method, such as a sweep of the V–P curve, can provide a more robust approach with higher speed and stability by periodically re-establishing the optimal operating point for the P&O's local search.

As illustrated in Fig. 3, the algorithm calculates the instantaneous power ($P_{[n]}$) from the acquired DC-link voltage ($V_{[n]}$) and current ($I_{[n]}$) data. The direction of the voltage perturbation (V_{ref}) is then determined by comparing this value with the previously obtained power ($P_{[n-1]}$). If the power change (ΔP) is positive, the perturbation continues in the same direction; otherwise, it is reversed. This process uses a fixed-step size, operating within the imposed voltage limits ($V_{curve} - U \leq V_{ref} \leq V_{curve} + U$, where U is an arbitrary fixed voltage value). In other words, the MPPT subsystem employs the traditional fixed-step P&O strategy to refine the search for the optimal DC-link voltage within the general vicinity of the maximum power point (MPP), established based on the V–P curve scan. Notably, this hybrid approach makes the tracking robust to changes in the overall characteristic curve shape.

To generate the DC-link P–V (power–voltage) curves, a computational model of the TGR unit was developed. Resistive loads, ranging from 10 Ω to 200 Ω, were connected to the system output to represent the equivalent load of the inverter operating at a unity power factor. Under a fixed streamflow, voltage and current measurements were recorded for each resistance value, after which the water speed was adjusted and the process was repeated to collect additional data.

Fig. 4 shows the curves for seven water speeds, which were determined using a third-order polynomial regression. Note that the specified DC-link operating voltage, which ranges from 340 V to 530 V, satisfies two key requirements. First, the minimum operating voltage is safely higher than the peak of

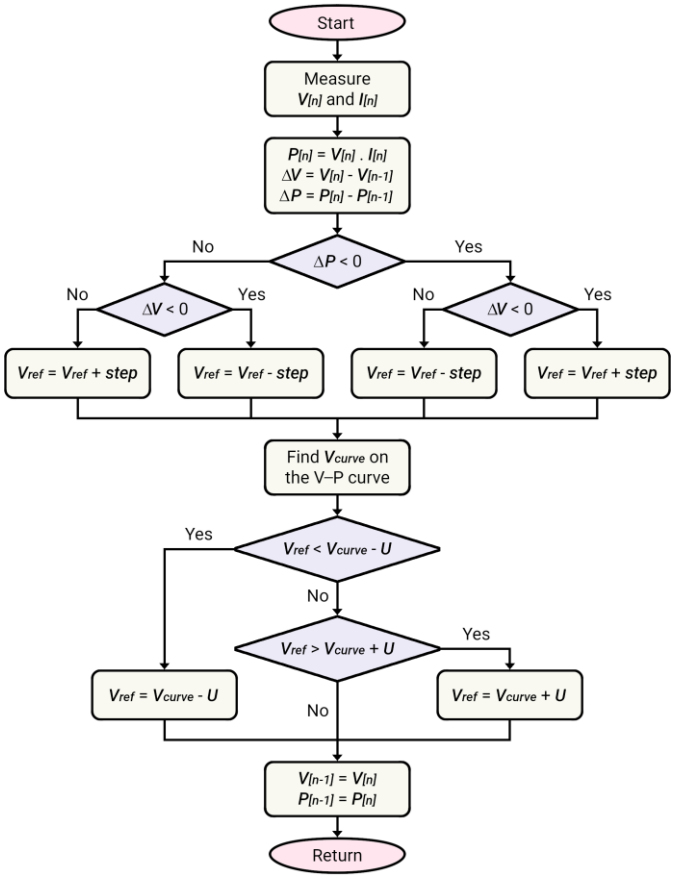

Fig. 3. Flowchart of the hybrid MPPT algorithm.

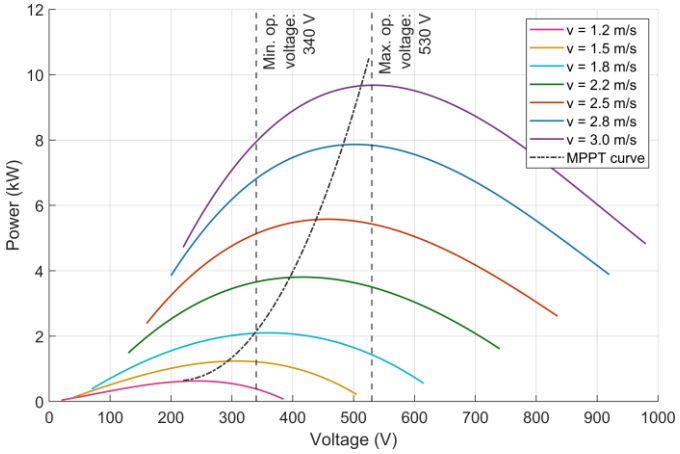

Fig. 4. P–V curves of the TGR unit for various water speeds.

the grid line voltage (311 V), preventing power reversal through the inverter's freewheeling diodes. Second, the maximum operating voltage is strategically set to be slightly greater than the voltage at maximum power point (V_{mpp}) under nominal conditions, but significantly lower than the overall capacity of the PEI itself.

A linear regression of the peaks from the multiple P–V curves yielded the plant's maximum power V–P curve, which is shown in Fig. 5. The coefficient of determination, nearly unitary ($R^2 = 0.9988$), indicated a strong fit.

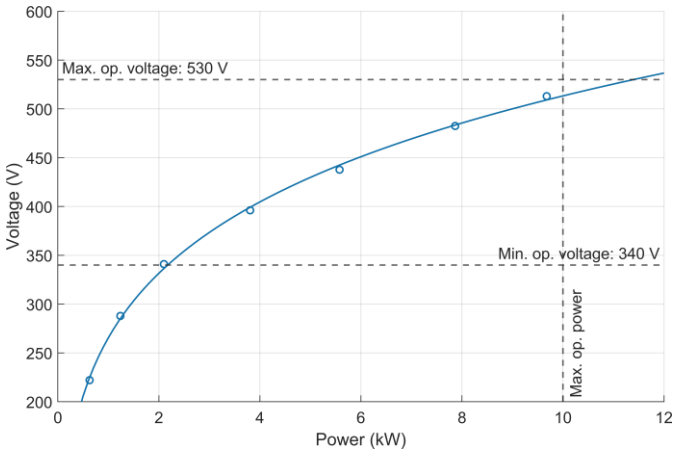

Fig. 5. V–P curve for maximum power of the TGR set.

Finally, using a power regression equation with 95% confidence bounds, the V–P curve is expressed as

$$V_{curve}(P_{DC}) = 228.9{P_{DC}}^{0.1452} - 358.7. \quad (13)$$

In the equation, V_{curve} represents the voltage for maximum power predicted by the curve model (V), and P_{DC} represents the instantaneous DC-link power (W).

The specifications of the open-channel hydrokinetic microgenerator's model developed on the computational platform are described in Table I.

TABLE I
SPECIFICATIONS OF THE OPEN-CHANNEL HYDROKINETIC MICROGENERATOR

Turbine parameters	
Type	Axial flow
Rotor diameter	1.55 m
TSR	1.79
Coef. of power	0.39
Rated flow	3 m/s
Transmission ratio	1:9
Generator parameters	
Type	PMSG
Output Power	10 kW
Rated voltage	440 V
Rated frequency	60 Hz
Rated speed	600 rpm
Number of phases	3
Connection type	Y (int. neutral)
Pole pairs	6
Stator resistance	0.4 Ω
Inductances d-q	8 mH; 8 mH
Inertia	0.015 kg·m^2
Viscous damping	0.0008 N·m·s
Rectifier parameters	
Configuration	3-phase full-wave bridge
Forward voltage (diodes)	1.6 V
Forward current (diodes)	6.7 A
Max. reverse voltage (diodes)	530 V
Capacitive filter parameters	
Voltage range	340 – 530 V
Capacitance	5.3 mF
Max. ripple voltage	1%
*Table I (cont.) →	

*Table I (cont.) ↓	
Inverter parameters	
Configuration	3-wire, 3-phase bridge
Type of transistors	IGBTs with antiparallel diodes
Switching frequency	30 kHz
Forward voltage (transistors)	1.6 V
Inductive filter parameters	
Inductance	1.2 mH
Internal resistance	0.1 Ω
Max. ripple current	4%
Grid parameters	
Voltage	220/127 V_{rms}
Frequency	60 Hz
Controller parameters	
MPPT sampling rate	4 Hz
MPPT step size	2.4 V
MPPT perturbation voltage range	20 V
Voltage sensor ratio	1/100
Voltage PI gains	kp = 13.0 ki = 344.8
Current sensor ratio	1/10
Current PI gains	kp = 39.0 ki = 1.059×10^6
Carrier peak (PWM)	20 V
Max. islanding detection phase angle	8°
Min. frequency deviation for islanding detection	1 Hz

V. Results and Discussion

This section presents the behavior of the hydrokinetic microgenerator's quantities under different scenarios. The simulation was performed using an MPPT sampling rate of 4 Hz and a step size of 2.4 V, with the inverter switching frequency at 30 kHz.

As displayed in Fig. 6, the predefined flow velocity initially increased from 2.2 m/s to a peak of 3.0 m/s before decreasing to 2.5 m/s over a 20-second interval. Fig. 7 shows the rotational speed, tip speed ratio, and power coefficient of the HKT. It illustrates the device's rotational speed for each input condition in a way to maintain the TSR near the ideal value of 1.79 and the C_p stabilized at its peak of 0.39.

The PMSG's phase voltage and current appear in Fig. 8. Observe that, due to the fluid's high density (1000 kg/m^3), slight variations in streamflow resulted in substantial changes in power generation. Another interesting point to note is how the amplitudes of these quantities adapted precisely to each input condition for tracking the maximum power point. In the zoomed-in sections, the waveforms can be analyzed in more detail when the machine was at its rated speed (600 rpm). At that moment, the stator current analysis revealed the total harmonic distortion (THD) of 19.14%. Arising from the 6-pulse passive rectifier, the 5th, 7th, 11th, and 13th order harmonics were found to have the most significant magnitudes in relation to the 60 Hz fundamental frequency, as shown in Fig. 9.

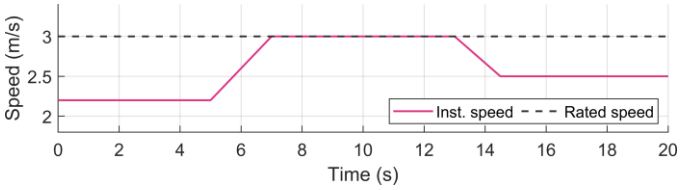

Fig. 6. Time-dependent flow condition.

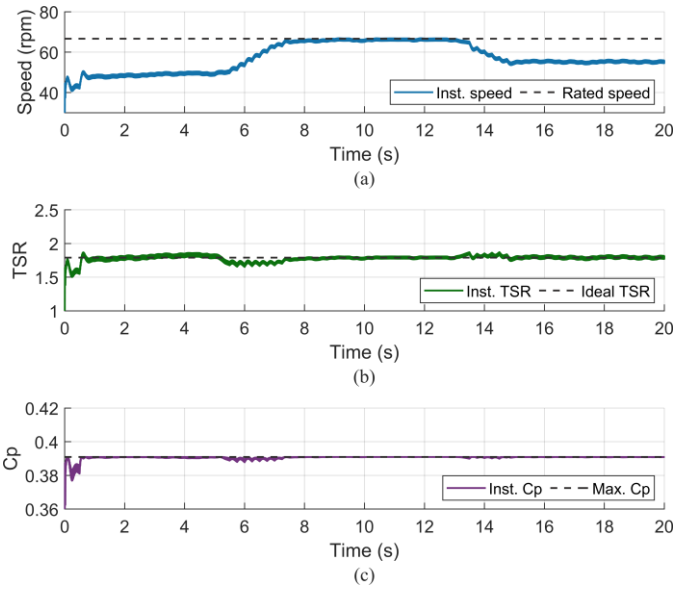

Fig. 7. HKT's response: a) Rotational speed, b) TSR, c) Power coefficient.

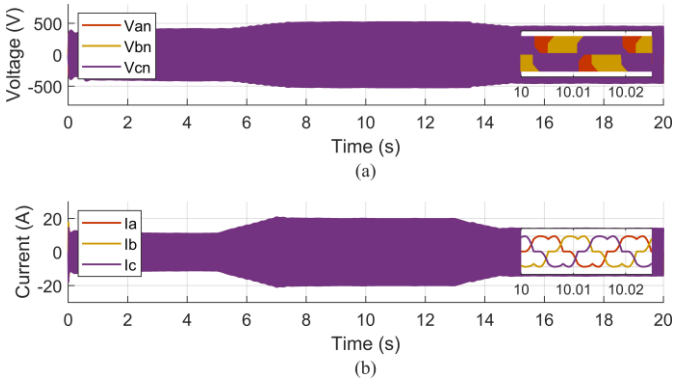

Fig. 8. PMSG's response: a) Phase voltage, b) Current.

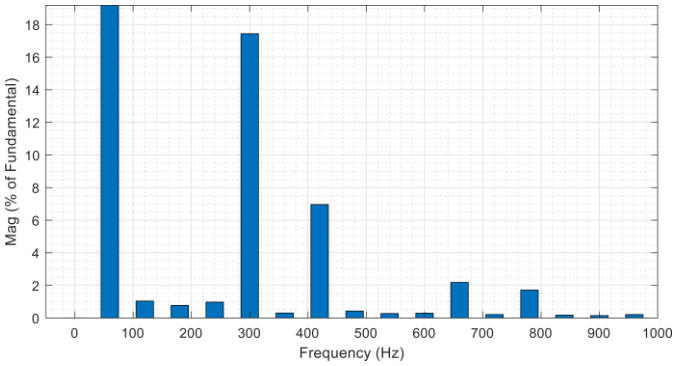

Fig. 9. Stator current harmonic spectrum.

Fig. 10 exhibits the power, voltage, and current of the rectifier output. It proves that the DC-link voltage (green line) closely tracked the MPPT subsystem's reference (red line), indicating compatibility with the outer loop's response. The magnified areas spotlight the ripple of the power and current curves, with peak-to-peak amplitudes of 2 kW and 4 A, respectively.

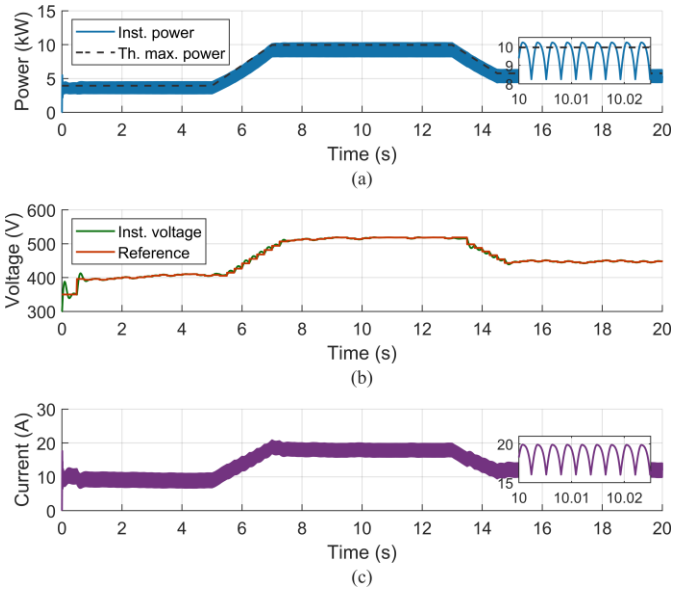

Fig. 10. Rectifier output: a) Power, b) Voltage, c) Current.

Fig. 11 highlights the behavior of the DC-link voltage (green line) controlled by the hybrid MPPT strategy. As seen, the reference (blue line) remained within the maximum (beige line) and minimum (yellow line) boundaries of the 20 V disturbance range (i.e., $U = 10$ V), which was defined based on the V–P curve (red line). Such limits ensured relative stability for the associated P&O method while enabling it to correct any deviations from the curve. The zoomed-in plot details the track during eight steps of the controller. By relating the generated energy to the theoretical maximum, the average tracking factor (TF) of 96.21% was obtained at the end of the simulation.

The output power and RMS current of the unit are shown in Fig. 12. The top graph indicates high energy conversion efficiency where the output power (blue line) is close to the theoretical maximum power (dashed line). The small decrease in delivered power during nominal condition, i.e., from 7 s to 13 s, is explained by the ohmic losses in the inductive filter, which are proportional to the square of the current. The bottom graph represents the typical operation of the voltage source inverter (VSI) in a current-controlled mode: injecting current into the grid according to the available energy.

An expanded view of the phase voltage and current at the point of common coupling (PCC) immediately following the 10-s mark is provided in Fig. 13. The synchronization of the sinusoidal waveforms confirms that the PEI was, as expected, operating at a nearly unity power factor (PF). The inset shows a ripple current of approximately 4%, within the predefined requirements.

Programming the MPPT subsystem exclusively with the V–P curve, i.e., without the P&O strategy, and performing the simulation for the same streamflow and sampling rate, the average TF of 96.14% was achieved. A 0.07 percentage point growth in the conversion rate suggests that the hybrid technique, by introducing the perturbation range, enhanced its robustness against potential inaccuracies in the modeled curve. Ultimately, the developed algorithm is not only fast and efficient but also capable of allowing for slight changes in the physical parameters of the generating unit without affecting the optimal operating condition.

In order to test the islanding detection feature, a parallel RLC load was connected to each phase at the PCC and tuned to a unitary quality factor ($Q_f = 1$), resulting in $R = 6.5\ \Omega$, $L = 17.1$ mH, and $C = 411\ \mu$F. With a constant water flow of 2.5 m/s, the grid disconnection was scheduled for 0.6 s. In the course of the simulation, islanding was detected within 155 ms based on a 1 Hz deviation from the nominal frequency (60 Hz), meeting the performance criteria for similar grid-tied systems. Fig. 14 details the plant output quantities throughout the test. Note that an overvoltage of up to 20% was recorded at the PCC in the power outage; however, given its short duration, the chances of the disturbance causing damage to the load are assumed to be remote.

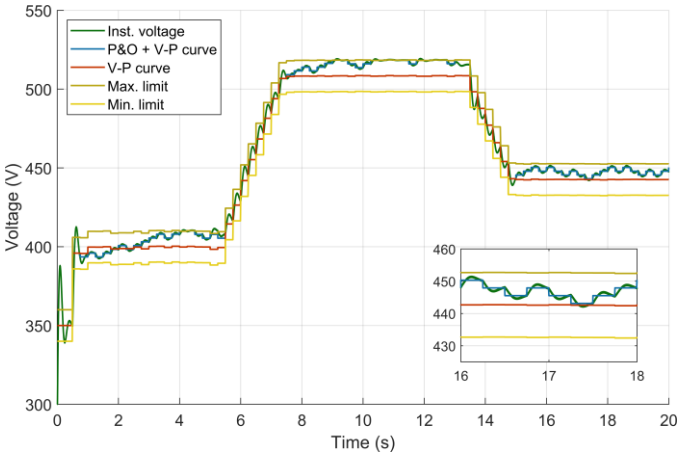

Fig. 11. DC-link voltage controlled by the hybrid MPPT method.

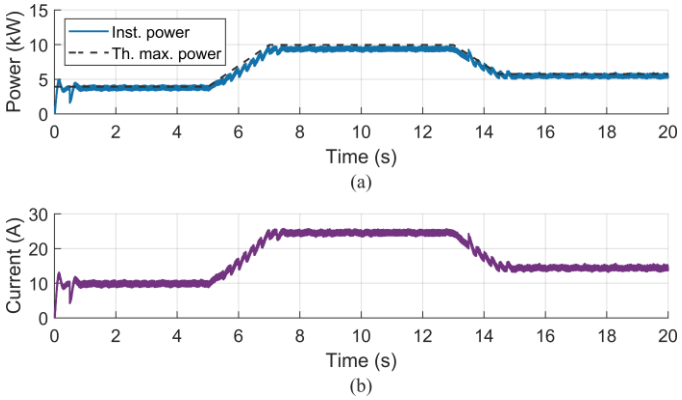

Fig. 12. System output: a) Power, b) RMS current.

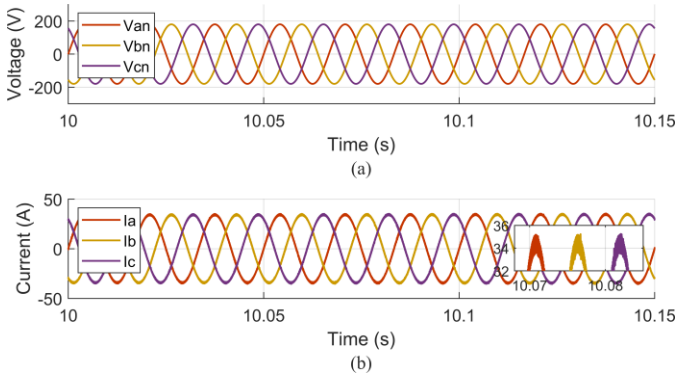

Fig. 13. Magnified view of the waveforms at the PCC: a) Phase voltage, b) Current.

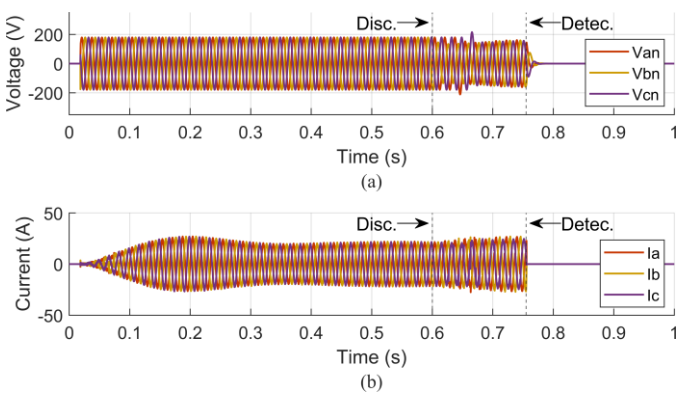

Fig. 14. System output during the islanding test: a) Phase voltage, b) Current.

VI. Conclusion and Future Work

This work addressed the development of a hybrid MPPT method for controlling an open-channel hydrokinetic microgenerator in grid-connected mode, aiming for maximum energy capture and operational reliability. The algorithm, which combines the traditional P&O strategy with the unit's V–P characteristic curve, was validated on the MATLAB/Simulink® platform under varying flow conditions. Quantitative analyses demonstrated that the proposed technique is agile and robust to curve inaccuracies and minor system parametric deviations (electrical and mechanical), all without compromising conversion efficiency.

Future work will focus on the following:

--Implementing the model on a reduced scale to validate the results.

--Investigating the impacts of integrating high-power-factor rectification structures into the topology.

References

[1] M. Sood and S. K. Singal, "Development of hydrokinetic energy technology: A review," *Int J Energy Res*, vol. 43, no. 11, pp. 5552–5571, Apr. 2019. DOI: 10.1002/er.4529

[2] M. Ridgill, M. J. Lewis, P. E. Robins, S. D. Patil, and S. P. Neill, "Hydrokinetic energy conversion: A global riverine perspective," *J. Renewable Sustainable Energy*, vol. 14, no. 4, 044501, pp. 1–17, July 2022. DOI: 10.1063/5.0092215

[3] H. J. Vermaak, K. Kusakana, and S. P. Koko, "Status of micro-hydrokinetic river technology in rural applications: A review of literature," *Renew. Sustain. Energy Rev.*, vol. 29, pp. 625–633, Jan. 2014. DOI: 10.1016/j.rser.2013.08.066

[4] M. J. Khan, M. T. Iqbal, and J. E. Quaicoe, "River current energy conversion systems: Progress, prospects and challenges," *Renew. Sustain. Energy Rev.*, vol. 12, no. 8, pp. 2177–2193, Oct. 2008. DOI: 10.1016/j.rser.2007.04.016

[5] R. Pudur and S. Gao, "Savonius rotor based grid connected hydrokinetic power generation scheme," *SEGAN*, vol. 5, pp. 148–155, Mar. 2016. DOI: 10.1016/j.segan.2015.12.004

[6] C. M. Niebuhr, M. van Dijk, V. S. Neary, and J. N. Bhagwan, "A review of hydrokinetic turbines and enhancement techniques for canal installations: Technology, applicability and potential," *Renew. Sustain. Energy Rev.*, vol. 113, 109240, pp. 1–18, Oct. 2019. DOI: 10.1016/j.rser.2019.06.047

[7] M. Ridgill, S. P. Neill, M. J. Lewis, P. E. Robins, and S. D. Patil, "Global riverine theoretical hydrokinetic resource assessment," *Renewable Energy*, vol. 174, pp. 654–665, Aug. 2021. DOI: 10.1016/j.renene.2021.04.109

[8] L. Cacciali, L. Battisti, S. Dell'Anna, and G. Soraperra, "Case study of a cross-flow hydrokinetic turbine in a narrow prismatic canal," *Ocean Engineering*, vol. 234, 109281, pp. 1–10, Aug. 2021. DOI: 10.1016/j.oceaneng.2021.109281

[9] M. H. Ashourianjozdani, L. A. C. Lopes, and P. Pillay, "Power control strategy for fixed-pitch PMSG-based hydrokinetic turbine," in *2016 IEEE International Conference on PEDES*, Trivandrum, India, Dez. 14-17, 2016, pp. 1–6. DOI: 10.1109/PEDES.2016.7914245

[10] P. B. Ngancha, K. Kusakana, and E. Markus, "Modelling and simulation of a power converter for variable speed hydrokinetic systems," in *2017 International Conference on the DUE*, Cape Town, South Africa, Apr. 4-5, 2017, pp. 227–232. DOI: 10.23919/DUE.2017.7931848

[11] F. A. M. Vásquez, T. F. de Oliveira, and A. C. P. Brasil Junior, "On the electromechanical behavior of hydrokinetic turbines," *Energy Conversion and Management*, vol. 115, pp. 60–70, May 2016. DOI: 10.1016/j.enconman.2016.02.039

[12] B. Kirke, "Hydrokinetic turbines for moderate sized rivers," *Energy for Sustainable Development*, vol. 58, pp. 182–195, Oct. 2020. DOI: 10.1016/j.esd.2020.08.003

[13] P. C. Krause, O. Wasynczuk, and S. D. Pekarek, *Electromechanical Motion Devices*, 2nd ed. New Jersey: John Wiley & Sons, Inc., 2012.

[14] R. G. Jordão, *Synchronous Machines*, 2. ed. Rio de Janeiro: LTC, 2013.

[15] I. Boldea, *Synchronous Generators*. Boca Raton: CRC Press, 2006.

[16] C. B. Albuquerque and F. A. M. Vásquez, "Modeling and control of isolated modular hydrokinetic energy systems," in *2021 WCNPS*, Brasilia, Brazil, Nov. 18-19, 2021, pp. 1–6. DOI: 10.1109/WCNPS53648.2021.9626272

[17] M. A. R. Shafei, D. K. Ibrahim, E. E. -D. A. El-Zahab, and M. A. A. Younes, "Biogeography-based optimization technique for maximum power tracking of hydrokinetic turbines," in *2014 ICRERA*, Milwaukee, WI, USA, Oct. 19-22, 2014, pp. 789–794. DOI: 10.1109/ICRERA.2014.7016493

[18] M. Wise, M. Al-Badri, B. Loeffler, and J. Kasper, "A novel vertically oscillating hydrokinetic energy harvester," in *2021 IEEE Conference on SusTech*, Irvine, CA, USA, Apr. 22-24, 2021, pp. 1-8. DOI: 10.1109/SusTech51236.2021.9467425

[19] R. -A. Chihaia, I. Vasile, G. Cîrciumaru, S. Nicolaie, E. Tudor, and C. Dumitru, "Improving the energy conversion efficiency for hydrokinetic turbines using MPPT controller," *Appl. Sci.*, vol. 10, no. 21, 7560, pp. 1–13, Oct. 2020. DOI: 10.3390/app10217560

[20] J. C. O. de S. Lescano, L. Galotto Junior, H. C. S. Souza, T. Estrabis, G. Gentil, and R. Cordero, "Modeling and simulation of a hydrokinetic generation connected to the electricity grid," in *XXIV CBA 2022*, Fortaleza, Brazil, Oct. 16-19, 2022, pp. 1466–1473. DOI: 10.20906/CBA2022/3374